

Combining X-ray Nano-CT and XANES Techniques for 3D *Operando* Monitoring of Lithiation

Spatial Composition evolution in NMC Electrode

Tuan-Tu Nguyen^{1,2}, Jiahui Xu^{1,3}, Zeliang Su^{1,3}, Vincent De Andrade⁵, Alejandro A. Franco^{1,3,4}

Bruno Delobel², Charles Delacourt^{1,3}, Arnaud Demortière^{1,3,4*}

¹Laboratoire de Réactivité et Chimie des Solides (LRCS), CNRS-UPJV UMR 7314, rue Baudelocque, 80039 Amiens Cedex, France.

²Renault Technocentre, 78084 Guyancourt, France

³Réseau sur le Stockage Electrochimique de l'Energie (RS2E), CNRS FR 3459, rue Baudelocque, 80039 Amiens Cedex, France.

⁴ALISTORE-European Research Institute, CNRS FR 3104, Hub de l'Energie, Rue Baudelocque, 80039 Amiens Cedex, France.

⁵Advanced Photon Source, Argonne National Laboratory, Lemont, USA.

Corresponding Author: arnaud.demortiere@cnrs.fr

ABSTRACT: In this study, we present a well-defined methodology for conducting *Operando* X-ray absorption near-edge structure spectroscopy (XANES) in conjunction with transmission X-ray nano computed tomography (TXM-nanoCT) experiments on the $\text{LiNi}_{0.5}\text{Mn}_{0.3}\text{Co}_{0.2}\text{O}_2$ (NMC) cathode electrode. To minimize radiation-induced damage to the sample during charge and discharge cycles and to gain a comprehensive 3D perspective of the (de)lithiation process of the active material, we propose a novel approach that relies on employing only three energy levels, strategically positioned at pre-edge, edge, and post-edge. By adopting this technique, we successfully track the various (de)lithiation states within the three-dimensional space during partial cycling. Furthermore, we are able to extract the nanoscale lithium distribution within individual secondary particles. Our observations reveal the formation of a core-shell structure during lithiation and we also identify that not all surface areas of the particles exhibit activity during the process. Notably, lithium intercalation exhibits a distinct preference, leading to non-uniform lithiation degrees across different electrode locations. The proposed methodology is not limited to the NMC cathode electrode but can be extended to study realistic dedicated electrodes with high active material (AM) density, facilitating exploration and quantification of heterogeneities and inhomogeneous lithiation within such electrodes. This multi-scale insight into the (de)lithiation process and lithiation heterogeneities within the electrodes is expected to provide valuable knowledge for optimizing electrode design and ultimately enhancing electrode performance in the context of material science and battery materials research.

KEYWORDS: nano-CT, *Operando* XANES-TXM, NMC cathode electrode, delithiation process, 3D dynamical process

Introduction

Over the last decades, with the increase in energy demand along with the shift towards greener energy solutions, lithium-ion batteries (LIB) have gained attraction for energy storage applications.^[1–4] As for many other electrochemical systems, porous structures are used for making LIB electrodes since they can tremendously increase the specific interfacial area between phases, which enhances the accessible capacity of the active materials (AM) at high C-rate. However, the hierarchical architecture of the electrode microstructure makes it challenging to achieve a homogeneous structure.^[5] Microstructural heterogeneities, which result from the non-uniform distribution of phases, can cause a non-uniform electrochemical behavior, deteriorating the electrode performance and leading to macroscopic failures.^[6–9] Therefore, identifying these heterogeneities and understanding their impact on the electrochemical performance is crucial to improve the electrode design.

Local electrochemical properties such as effective ionic conductivity and charge transfer impedance are not trivial to measure using traditional electrochemical methods. In an attempt to overcome this challenge, Forouzan *et al.*^[7a] considered an approach that involves an inverse correlation between local electronic and ionic conductivities, in which the carbon binder domain (CBD)^[7b] additive mixture increases both the electronic conductivity and tortuosity^[7c] of the ionic conducting pathway with its nano-porosity. They measured the local effective electronic conductivity through a μ 4-lines system, allowing them to qualitatively correlate the electrode microstructure with its effective transport properties.

Various other techniques such as Raman microscopy^[16], X-ray diffraction (XRD)^[17,18], X-ray Absorption Spectroscopy (XAS)^[19], or 2D X-ray absorption near-edge structure spectroscopy (XANES)^[19–22] can be employed to investigate the reaction distributions in composite battery electrodes. However, these methods are limited to 2D observation, as the obtained signal is integrated spatially along the depth direction. Consequently, accurate capture of the 3D spatial distributions is not possible, which may result in incorrect interpretation of the mechanism due to the difficulty in uniquely interpreting complex 3D structures based on projected images.^[23a, 23b]

Previous studies have extensively employed a multimodal approach that combines electrochemical measurements with X-ray tomography techniques to investigate microstructural properties of electrodes, despite significant efforts for the setup preparation as well as the data post-processing^[10–15b]. For instance, Finegan *et al.*^[24] recently utilized *Operando* X-ray diffraction-computed

tomography (XRD-CT) to characterize the dynamic crystallographic structure within and between LMO particles during operation in 3D. This approach enables the identification of stoichiometric and phase heterogeneities within particles and/or the bulk electrode, and therefore the reaction distribution can be inferred.

Several authors have employed X-ray absorption near-edge spectroscopy (XANES) and X-ray tomography to generate a comprehensive dataset that enables direct correlation of chemical information and microstructure. For instance, Meirer *et al.* utilized 3D XANES to investigate the conversion of NiO to Ni metal in a partially reduced electrode. Their findings revealed significant size-dependent inhomogeneities in the chemical states throughout the particle, as well as evidence of fracturing caused by volume expansion during the reaction. Wang *et al.* more recently conducted a study in which they collected a 46-point spectrum across the iron K-edge of a LiFePO₄ cathode particle and created a run-out correction system that enabled automated tomography. The study yielded remarkable insights, such as the emergence of a clear core-shell structure. Tan *et al.* [25] utilized XANES in combination with transmission X-ray computed tomography (TXM-CT) in an *in situ* experiment on a pouch cell to investigate the heterogeneities resulting from its initial delithiation. Similarly, Kimura *et al.* [26] employed CT-XANES to perform 3D *Operando* imaging of the mesoscopic inhomogeneous electrochemical reaction in a composite solid-state battery electrode and visualized the 3D inhomogeneous reaction evolution during (dis)charge.

Nano-CT electrochemical *Operando* measurements pose significant challenges to imaging experiments, particularly in terms of spatial, chemical, and temporal resolutions. The duration of many battery reactions is quite long, often spanning several hours, but it's essential to collect at least five data points during the reaction to build a reaction pathway. However, this requirement imposes limitations on the available time to complete an image that contains the desired chemical information at the desired level of spatial resolution.

Unfortunately, all modes of chemical contrast require collecting multiple frames for the same reaction state to reconstruct a map of the species present in the field view. For instance, XANES microscopy achieves chemical resolution by collecting frames at a large number of energies, limited by the precision of the upstream optics. In practice, researchers typically opt to minimize the number of points required to achieve some level of chemical resolution in the individual frameset by scanning energy.

Most previous works on *in situ/Operando* experiments [20,27,28], whether using 2D XANES or XANES-TXM, have utilized electrodes with a low loading of active material and a low AM density (approximately %v AM = 20%). This approach helps to avoid overlapping issues during 2D XANES experiments, where

depth information is lost as it is combined into one projection, while also allowing for high X-ray transmission during acquisition to maximize the signal-to-noise ratio. However, using these types of electrodes limits electrochemical performance to solid diffusion in the AM particles rather than porous-electrode effects.

In this study, we present a new method for capturing electrode microstructure during high-rate electrochemical operation to provide a more efficient approach for investigating the effects of microstructural heterogeneities on electrochemical performance. We conducted XANES-TXM-CT experiments in *Operando* mode at the nanoscale to investigate NMC-532 positive electrodes using electrochemical cell designed for tomography constraints. Performing experiments in *Operando* mode provides significant advantages over *ex situ* approaches as the battery remains functional during the experiment, allowing for the characterization of microstructure and electrochemical behavior, including transport properties and reaction kinetics, at nanoscale resolution. To the best of our knowledge, this is the first attempt coupling nano-XCT and XANES techniques to characterize electrodes that are similar to real-life designs (with %v AM > 60%) along with a high operating current density.

Results

Figure 1 demonstrates the principles, apparatus, methods and samples of the *Operando* experiment. The workflow used in this work is illustrated in Figure 1a. Two reference XANES were obtained at Ni K-edge for electrode at pristine (stoichiometry Li = 1) and delithiation state (*ca.* stoichiometry Li = 0.38). Three energy levels: pre-edge, edge, post-edge, were selected, at which three tomography datasets are obtained. The 3D map of Li concentration distribution can be extracted via the relative shift of the absorption edge, which reflects the shift of Ni oxidation state from NMC with primarily Ni³⁺ in a pristine state to NMC with primarily Ni⁴⁺ in a delithiation state (see details in Methods section).

The Figure 1b, c and e show the devices applied in the experiment. The *Operando* electrochemical cells used in this work consist of a stainless-steel cover, a movable stainless-steel disc in the middle and a Teflon base, which can minimize the dead angles obscuring X-ray and is not operationally complicated. A detailed description of this cell can be found in an article previously published by our group^[29]. Two different electrodes that have similar AM density as real-life applications but have different AM loadings are utilized: the thinner electrode (Figure 1f), labelled as MX-A (AM loading = 3 mg/cm²), is made to facilitate the transmission of the X-rays through the sample without any further preparation steps as for higher AM loading electrode (AM loading = 15 mg/cm²), labelled as MX-B (Figure 1g). Several circular

patterns with diameters smaller than the field of view were laser-cut (as shown in Figure 1d) as experimental recording regions.

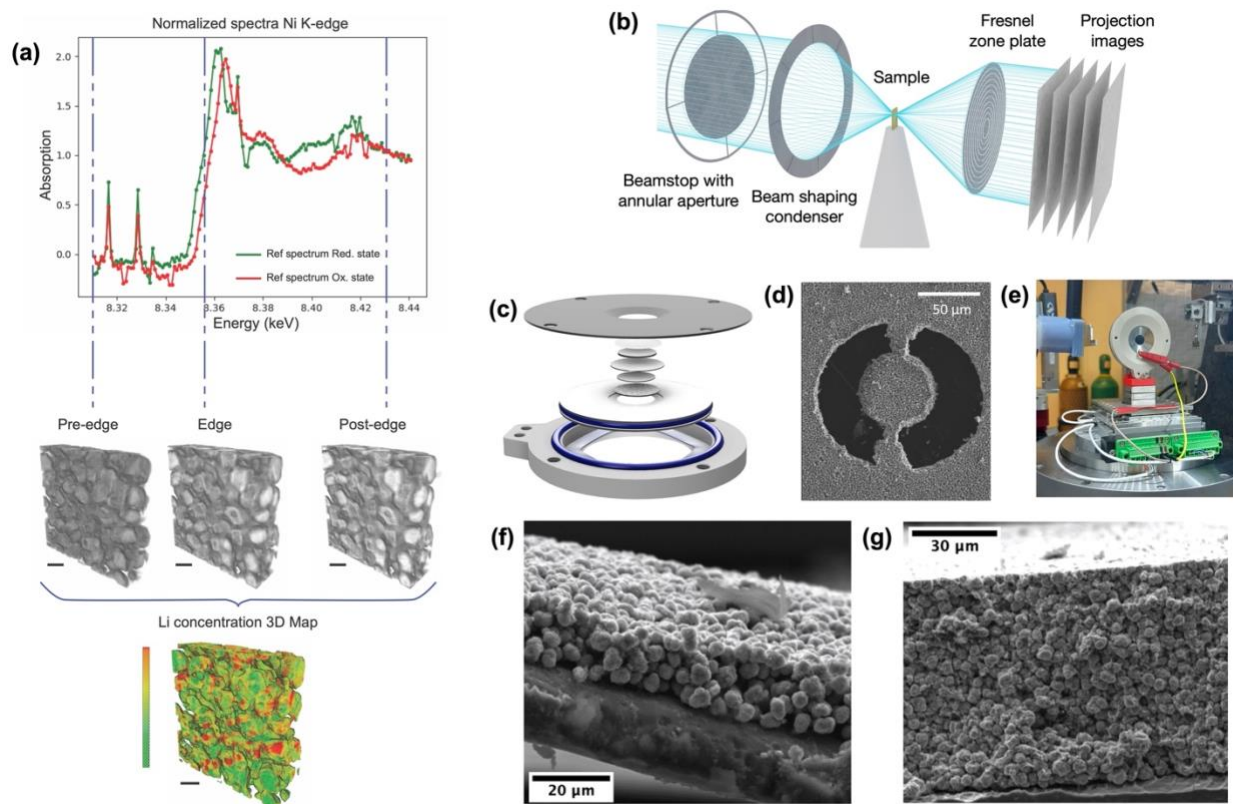


Figure 1. Illustration of the workflow, apparatus and samples used for this study. a) Our approach for Li concentration mapping based on three energy levels. The scale bar in **a** represent 10 μm. **b)** Schematic representation of the hard X-ray nano-holotomography experimental setup. **c, e)** The two Operando electrochemical cells used in this work. **d)** Electrode pattern cut by laser, as the region of study. **f)** Electrode with low mass loading (MX-A). **g)** Electrode with high mass loading (MX-B).

Within the cycling range between 2.5-4.3 V, Bak *et al.* reported that Ni is the predominant redox partner for lithium (de)intercalation in NMC, without any reactivities from Mn or Co having been witnessed.^[30] Hence, the Ni K-edge (Figure 1a) was selected to track the local Li content in the active material particles, as the Ni edge is the most sensitive to the local electrochemical reactions (compared with Mn and Co).

Depending on the Ni oxidation state, the AM can exhibit a change in X-ray absorption coefficient at the K-edge leading to a change of voxel intensity in the images. In spite of minor fluctuations at the pre-edge and post-edge energy, the AM keeps a stable interaction with the X-rays. This results in an invariance of intensity regardless of the Ni oxidation state. Figures 1a shows the 3D volumes obtained at the X-ray energies of 8.30 keV (pre-edge), 8.35 keV (edge) and 8.43 keV (post-edge), respectively. As shown in these

figures, an almost uniformly dark image was obtained when the X-ray energy was 8.30 keV. On the other hand, in the image obtained at 8.43 keV, the region where Ni was present showed a higher brightness. Edge absorption features (either edge position or peak top position) in the Ni K-edge have been shown in the literature to be approximately linearly correlated to Li content in NMC particles.^[31,32] Thus, by following the relative change of the absorption coefficient at the edge level normalized by the absorption jump (gap between the pre-edge and post-edge's absorption coefficient), one can infer the local Li concentration at each voxel with a simple linear correlation. As a result, a 3D map of the Li distribution throughout the control volume can be derived.

It is worth mentioning that two different electrochemical cells (Figure 1f, 1g) were used to carry out the *Operando* experiments in this work. The AMPIX cell,^[33,34] developed by Argonne National Laboratory, allows *in situ* experiments including multiple synchrotron-based X-ray scattering and spectroscopy methodologies to be performed. However, it is not fully compatible with the setup for TXM experiment (*e.g.*, high thickness, low open-angle) leading to high dead-angle during the acquisition. To minimize the dead-angle that increases with the sample thickness, the AMPIX cell was only used for the thinner electrode, MX-A.

On the other hand, a new cell design has been developed that better satisfies the requirements for TXM experiment giving high-quality tomographic data. Several features are optimized that allow the use of higher loading electrodes MX-B (loading AM = 15 mg/cm²) such as the cell thickness and the open-angle. The cell design is closely mirroring coin cell conditions, so that ensures good stack pressure as well as proper electrochemical functionality.

Thinner electrode MX-A

Given that the same region was monitored throughout the experiment, Figure 2 shows the 3D Lithium concentration maps during the lithiation process with a current density of 2 mA/cm². The overall Li concentration increases, as the experiment goes from state I to IV, seen by the fact that the shading of each map turns reddish on average. It is shown an increase of the number of Li-rich regions along the lithiation process, which are, however, not well-dispersed throughout the volume (denser accumulation of Li-rich regions can be observed at the front-right corner of the electrode).

The 2D slices are also shown in Figure 3 a, b, c, d for the ease of visualization. Overall, it can be seen that the core-shell structure is formed as the lithiation progresses. This result demonstrates that the Lithium intercalation starts first at the particle surface and moves toward the particle center as lithiation

progresses, which is consistent with the results in [16]. However, it is worth noting that not all the particle surface area is active, as further discussed when zooming in on individual AM particles (Figure 3e).

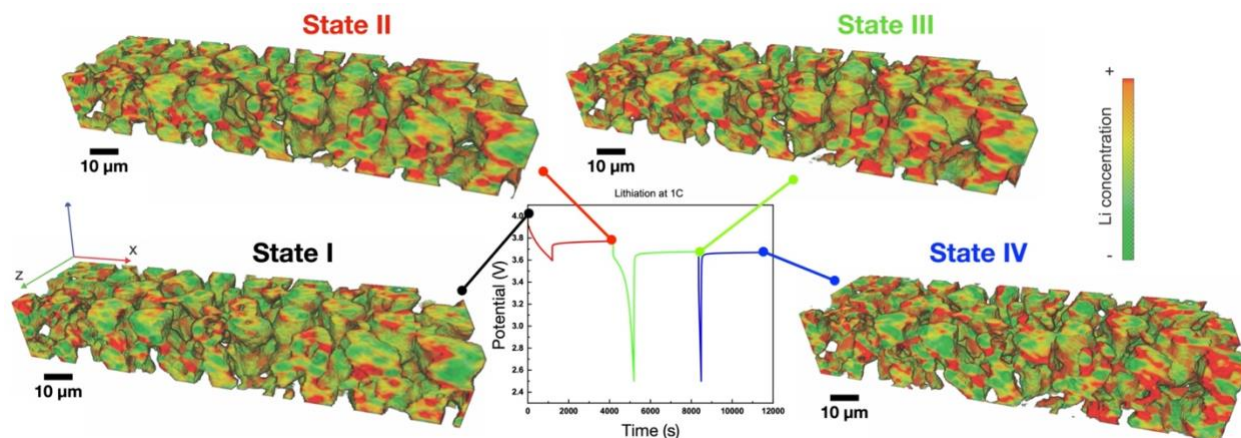


Figure 2. 3D lithiation spatial composition evolution of thin electrodes MX-A. The 3D map of Li distribution extracted from the XANES-TXM performed at the end of the relaxation steps that correspond to state I to IV. The color-bar indicates the lithium concentration. The scale bars represent 10 μm . The galvanostatic curves at different state of charges with relaxation points.

The heterogeneity of Li spatial distribution can be investigated through the distribution of the absorption coefficient at each voxel, as it is directly related to the Li content at the voxel. A shift of the absorption coefficient to a higher value is found as the lithiation occurs, in agreement with the XANES theory (Figure 1a). Besides, one can notice a large polarization appearing during the lithiation process (green and blue curves in the discharge curve in Figure 2). It is possible that this large polarization stems from the use of AMPIX cell along with too low electrode thickness. According to the AMPIX design, an annular flat gasket is used as a means to accommodate battery stacks having a typical thickness of *ca.* 800 μm , which is significantly higher than the battery stack used with MX-A (*ca.* 400 μm for MX-A with aluminum current collector/Glassy fiber/Li foil). This can deteriorate the role of the ‘spring’ resistance necessary for controlling the application of stack pressure of the gasket, leading to higher polarization.

Figure 3e shows a zoom on the Li concentration evolution within the two particles as the lithiation proceeds. Notably, a heterogenous Li distribution is observed inside both particles as the Li front moves toward the particle center. This observation is consistent with other works using $\text{LiNi}_x\text{Mn}_y\text{Co}_{(1-x-y)}\text{O}_2$ as AM,^[28,35] in which a heterogeneous Li distribution within the secondary particles was also witnessed.

On the left of Figure 3a-3d highlight the Li-rich areas (in red), which mainly establish at the vicinity of the particle surface area during the lithiation process. These regions are not uniformly distributed over

the particle surface area. Thus, Li intercalation is likely to occur at some preference sites. This might be attributed to the non-uniform distribution of phases such as the pore network or the CBD, which can impact the ionic/electronic transport to the reaction sites. On the other hand, the aspherical geometry of the AM particle can lead to nonuniform reaction distribution, which have been reported by Mistry *et al.*^[36] through physics-based calculations recently. Furthermore, the distribution of Li-rich regions at the AM particle surface might question the assumption used in macro-homogenous battery models that considers the entire particle surface area as available for reactions. Our next step will be to capture the presence of the CBD to understand further its role in the distribution of the reaction sites at the surface of the particles.

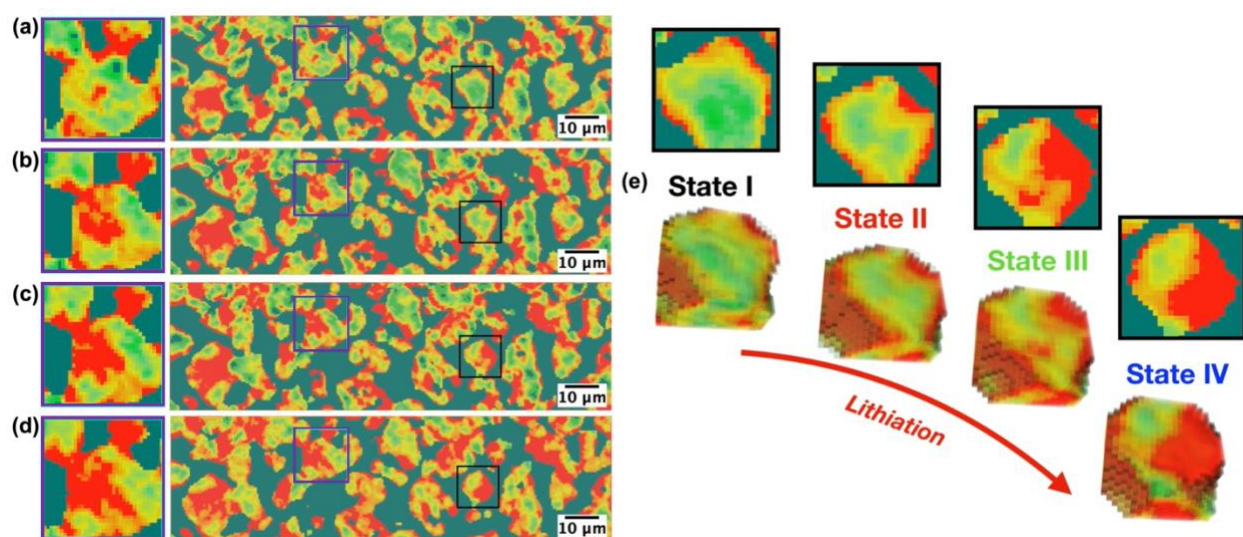


Figure 3. Zoom on the individual NMC secondary particles across the lithiation process. a-d) Cross-sectional map of Li concentration evolution from State I to IV. The area in purple boxes is magnified to the left **e)** Repartition of the Li-rich regions (in black) at each state of lithiation (I-IV) inside an individual secondary particle.

Individual particles were labeled and studied as shown in Figure 4a. When comparing the lithium concentrations within individual particles, as shown in Figure 4b, the volume fraction of Li rich part increases as the discharge process lithiates the particles. This kind of change occurs simultaneously within particles of different sizes. At the same time, there is a small increase in the size of the AM particles due to the Li embedding. There is some inaccuracy in this statistic due to the difficulty in labeling different particles as the increased AM particle contact after the calendaring process and the existence of cracks inside the particles. The distribution of Li contents of different states is further confirmed in Figure 4c. It quantifies the volume fraction of three classes relying on their Li content: Li rich (where $0.9 \leq$ absorption coefficient), Li moderate (where $0.6 < \text{absorption coefficient} \leq 0.9$), and Li poor (where absorption

coefficient ≤ 0.6), respectively. The volume fraction of Li-rich increases with the lithiation, and the volume fraction of Li-poor decreases.

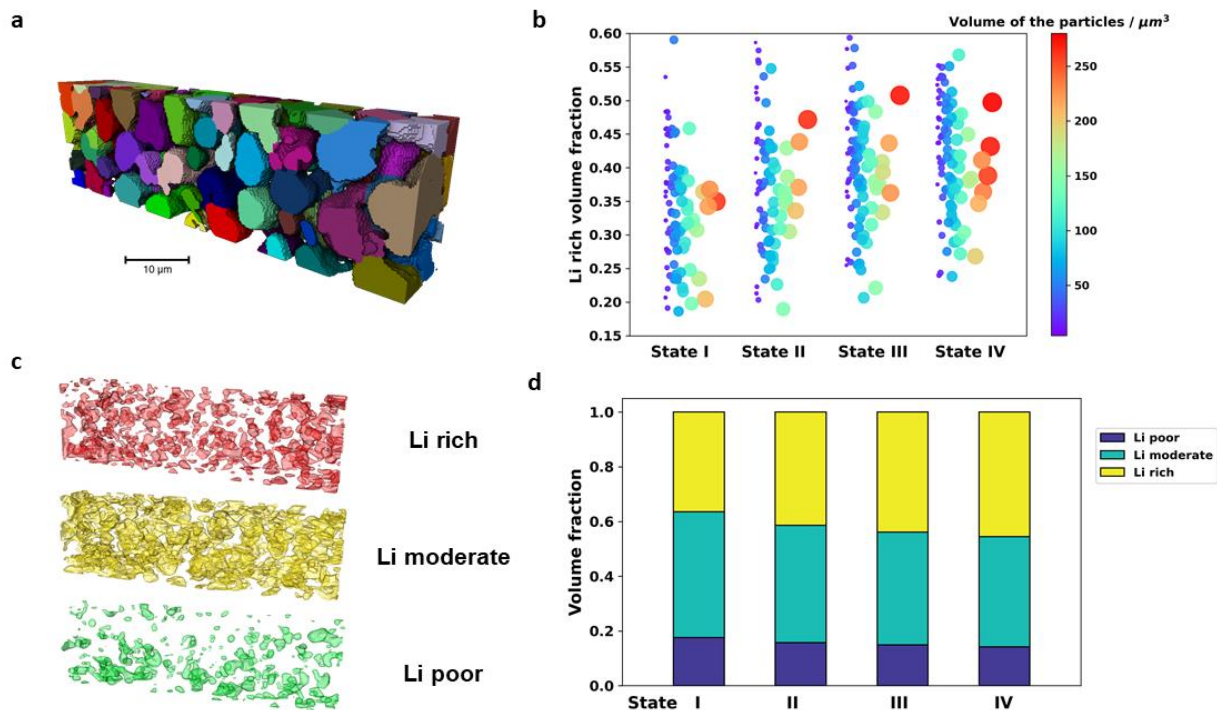


Figure 4. Statistical study on individual particles and total volume. a) The individual particles in the 3D volume were labeled. b) The graph represents how the Li rich volume fraction of different particles distribute in a different state of lithiation (I – IV). c) The distribution of the Li rich, Li moderate and Li poor phase. d) The bar graph shows the total Li contents extracted from the 3D quantitative analysis.

High loading electrode MX-B

An industry-graded electrode with a substantial AM loading is subsequently investigated to reflect real-life scenarios better. Consequently, more limitations from the porous microstructures leading to higher non-uniformity of electrochemical behavior due to porous-electrode limitations are expected.

The electrode was charged by constant current constant voltage (CCCV) at *ca.* $C/10$ up to 4.3 V and relaxed (Figure 5b). Before the charge, the pristine electrode bears a uniform Li distribution throughout the volume (Figure 5a). Figure 5c shows the final Li concentration at the lithiation state that corresponds with the Open Circuit Voltage (OCV) equals 4.2 V at a different position than State I. Despite a moderate discharge rate along with a CV step, there still are regions having high Li concentration, *i.e.* electrochemical reactions might not take place in these regions. Still, we remarked a shift to a more oxidation state of AM compared to state I (the majority is colored in green instead of red).

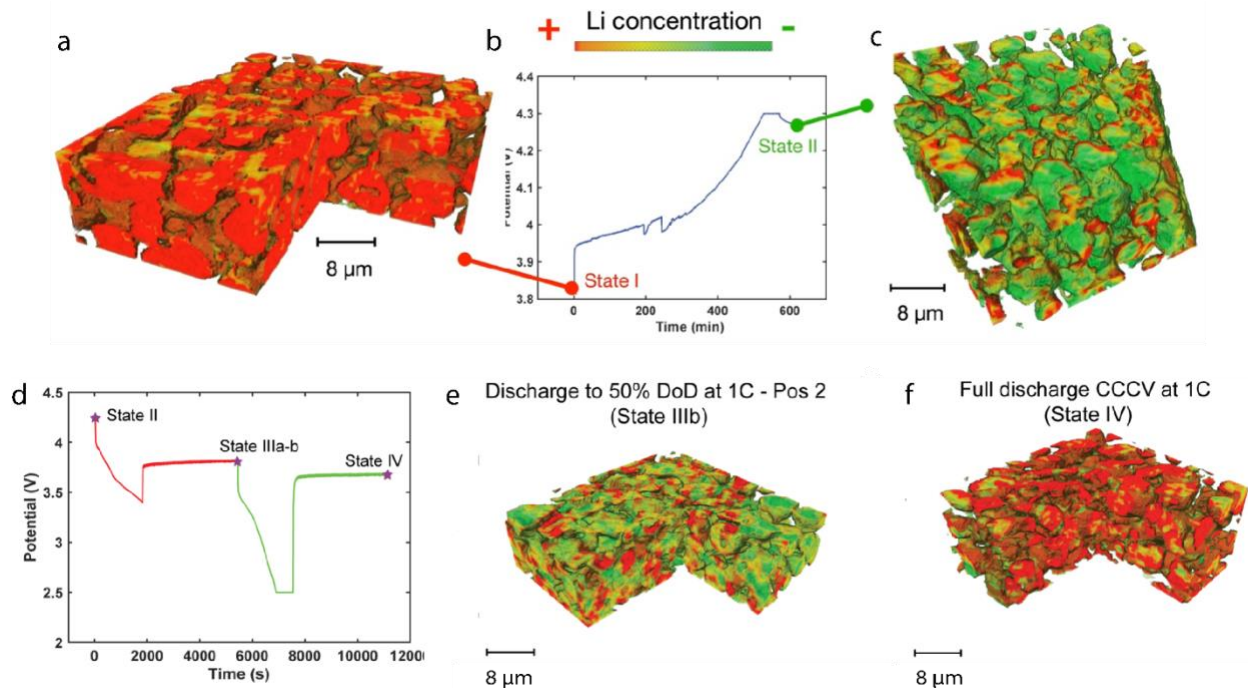


Figure 5. Results of thick electrode MX-B using our *Operando* cell during electrochemical cycling. **a)** The 3D map of Li concentration at the pristine state of the electrode before charging. **b)** The measured cell potential during the CCCV charge at C/10. The two XANES-TXM measurements are performed at points colored in purple. **c)** The 3D map of Li concentration extracted from the XANES-TXM performed at the end of the relaxation step after reaching 4.3 V with a CCCV. **d)** The measured cell potential during the CC discharge at 1C. The three XANES-TXM measurements are performed at points colored in purple. **e, f)** The 3D map of Li concentration extracted from the XANES-TXM performed at the end of the relaxation steps corresponds to different states of lithiation. The scale bars represent 8 μm .

The discharge process is shown in Figure 5 d-f. It consists of two separate steps, starting from state II discharge to 50% Degree of Discharge (DoD) and from 50% DoD discharge CCCV to 2.5 V. We decided to reduce the number of acquisition points compared to the case of the thin electrode because there was an important movement of the microstructure during the acquisition. This makes the data processing cannot be ensured as the alignment would be challenging. Figure S1 clearly shows the detachment of the AM particles between two TXM acquisitions.

At 50% DoD, two different locations that went through the same lithiation process (state III) are shown in Figure 6. From the 3D map of Li concentration (Figure 6a and 6b), position a has a higher Li concentration than position b. It also can be seen from Figure 6c that the Li content of a single AM particle in position a is higher than that in position b on average, despite undergoing the same discharge process. This is evidence for electrochemical heterogeneity occurring across the electrode during the battery

operation. As shown in Figure 6d, the average particle size at position b is higher than a, and the distribution of particle size leads to the difference in local porosity and the speed of lithiation.

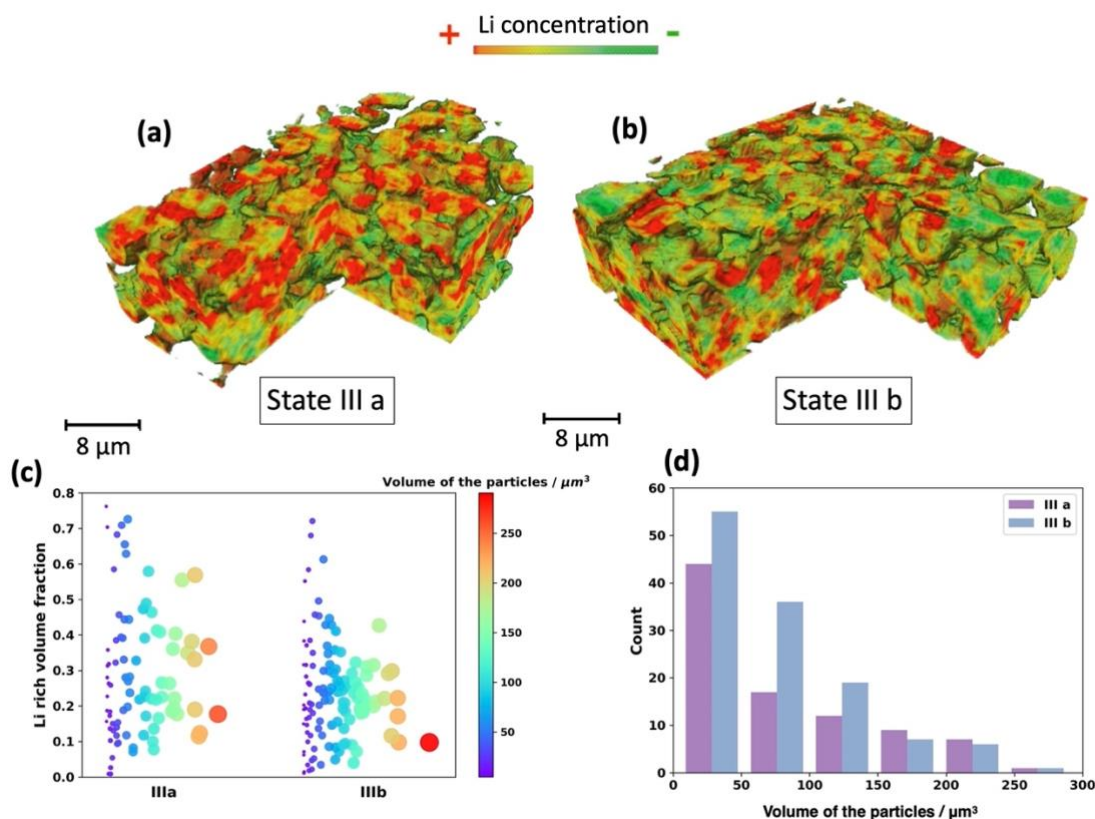


Figure 6. Heterogeneity of the electrodes at the same discharge state. a, b) The 3D map of Li concentration extracted from the XANES-TXM performed at state III. The scale bars represent 8 μm. c) The graph represents how the Li rich volume fraction of individual particles distribute in different positions at state III. d) Individual AM particles volume distribution.

Overall, the Li content at each state shows a good agreement with the expected values inferred from the electrochemical process. That is, a significant decrease of Li content at the end of the delithiation step then the Li concentration increases as we switch to the lithiation process. This is also confirmed in the bar graph, which compares the difference in Li content between different states (Figure S2a). Notably, the last step, after 1 hour of lithiation at 1C, shows a composition of Li concentration that is very close to the pristine electrode (Figure 5f and 5a).

Besides, the heterogeneity of Li content is also quantified, as shown in Figure S2. The distribution of voxel grey level is plotted, which is tantamount to the distribution of Li content presented within the volume. The pristine electrode exhibits essentially uniform Li content, as the distribution represents a sharp peak. In contrast, at the end of the first charge, the electrode (Figure 5b) possesses a heterogeneous Li concentration (broader distribution), where regions with high Li content are still present. Furthermore,

position 1 also exhibits a higher uniformity of Li content than in position 2 after undergoing the same discharge condition. Interestingly, despite the good agreement of the overall Li concentration at the end of the lithiation process, the electrode (Figure 5f) bears a higher non-uniformity of the Li content when compared to the pristine state.

To quantitatively analyze the distribution of Li concentration in the thickness direction, we calculated the average Li content in each 2D slice in the through-plane direction (Z-axis) and plotted it as a function of distance in Z-axis (shown in Figure S3). Pristine electrode (State I) shows a uniform high Li concentration across the thickness. In essence, the average Li content was not significantly changed in the thickness direction. The orientation of the thickness cannot be detected with our cell design. It should need further investigation in order to capture the electrochemical reaction evolving across the electrode thickness, which is crucial to investigate the effects of the porous electrode on the performance (*i.e.* transport in the liquid phase).

Discussions

In this work, we demonstrate that *Operando* XANES-TXM nanoCT allows access to the Li distribution (local Li concentration) at nanoscale within the LIB electrodes during the operation. We also proposed a method that relies on just three energy levels located at pre-edge, edge and post-edge for minimization of radiation damage to the sample (see more details in Methods). Also, a specific electrochemical cell and a sample preparation process were introduced, which make the use of electrodes typical to those used in real-life applications possible. This is crucial for our study where our goal is to focus on the impact of the microstructure on the electrochemical performance at electrode scale rather than the composition distribution within an individual AM particle, as reported in previous works.

With the addition of three-dimensional capability, both microstructural and chemical properties are obtained for a given large control volume, avoiding an overlap of contributions to the attenuation and providing the opportunity to probe the sample at different locations throughout the electrode.

Our experimental results unveil the non-uniformity of the Li repartition throughout the LIB porous electrodes during operation. Besides the core-shell structure found within the AM particles arising from the solid diffusion, the heterogeneity mainly reflects the microstructural heterogeneity, that can locally impact the kinetics of the electrochemical reactions through a non-uniform distribution of whether ionic/electronic transport network or inter-connectivity between phases throughout the electrode. As a result, there are regions being more active than the others as well as preference spots on the particle surface where the reactions are more likely to occur.

The Li repartition across the electrode depth is adequately uniform, which indicates a negligible effect from porous electrode. This is expected as we used ethylene carbonate: dimethyl carbonate (EC: DMC) solvent-based electrolyte at 1.2 M which reduces the limitation from ionic transport in liquid phase within the porous electrode. Thus, we can conclude that mass transport in the electrolyte is not a rate limiting factor in this electrode under the applied cycling conditions.

However, without a knowledge of the CBD morphology in the microstructure, it is not possible to accurately address the correlation between the accurate microstructure to the electrochemical heterogeneity, as the CBD can affect most of the microstructural properties such as transport properties, active electrochemical surface area. Thus, our next step is to capture the CBD morphology, which would allow the determination of all the microstructural properties with their spatial distribution (e.g. electronic conductivity, ionic tortuosity factor, triple-phase boundary). The distribution of electrochemical performance can, therefore, be fully resolved.

In addition, some of the reconstructed slices also revealed that the lithiation process could also happen from the internal pores of the AM particles. This observation also implies that the electrolyte along with the carbon conductive can penetrate into some internal pores through the AM grain boundaries and allow the (de)lithiation process to occur from the inside of the NMC secondary particles. This observation is in line with our previous work, in which we observed the occasional presence of the CBD inside the internal pores as well as the work done by Miller *et al.*,^[37] who revealed the penetration of electrolyte through the AM grain boundaries.

Nevertheless, there is a certain amount of dead angle in the cell during the tomography, which may affect the accuracy of the reconstruction. We are currently unable to determine the bias this causes in the analysis of lithium concentration, and further investigation is required. Therefore, it is also a direction in which the community must focus in order to eliminate the effect of dead angle on the reconstruction.

We expect that our analysis technique will provide a direct method to unveil the effects of the electrode microstructure on its electrochemical performance. This multiscale insight can shed light on the optimization of the electrode design to improve the electrode performance.

Conclusions

In conclusion, our study utilized *Operando* X-ray absorption near-edge structure spectroscopy coupled with transmission X-ray nano computed tomography (XANES-TXM nanoCT) to investigate the Li

distribution within NMC-532 cathode electrodes during charge and discharge processes. The Li content showed agreement with expected values, exhibiting a significant decrease during delithiation followed by an increase during lithiation. Heterogeneity in Li content was observed, with regions of higher concentration present after the first charge. The lithiation process displayed a non-uniform distribution of Li content compared to the pristine electrode. The electrode depth showed uniform Li repartition, indicating negligible effects from the porous electrode. However, understanding the correlation between microstructure and electrochemical heterogeneity requires further investigation, particularly regarding the CBD morphology. Internal lithiation from the AM particle pores was observed, indicating electrolyte penetration through AM grain boundaries. Additionally, observations of lithiation from internal pores of active material particles suggest electrolyte penetration through grain boundaries, influencing (de)lithiation processes. While our analysis technique offers valuable insights into electrode microstructure and electrochemical performance, further investigation is necessary to address dead angle effects during tomography reconstruction. Overall, our multiscale approach provides a direct method for understanding electrode microstructure effects on electrochemical performance, contributing to the optimization of electrode design and enhancing battery performance.

Method Section

Materials

Two positive electrodes investigated are both a mixture of $\text{LiNi}_{0.5}\text{Mn}_{0.3}\text{Co}_{0.2}\text{O}_2$ (NMC) as AM, conductive carbon black and a mixture of polyvinylidene fluoride (PVdF) with the same composition (96%w AM, 2%w carbon black and 2%w PVdF) but different AM loading. Electrode labelled as MX-A is made in our laboratory having a very low loading (*c.a.* 3 mg/cm^2) with 30% of porosity after calendaring. The second electrode labelled as MX-B is a commercial electrode with a loading of 15 mg/cm^2 and 28% of porosity after calendaring.

Apparatus preparation

Our setup requires the X-ray to go through at least the entire thickness of the electrode, as the travel pathway increases as the rotation angles move between $[-150^\circ, 150^\circ]$ (assuming that the glassy carbon windows, the Celgard 2500 and the Li foil are mostly transparent). Since it is a transmission technique, it is necessary to have enough X-rays going out of the sample to have enough signal on the detector. For the two electrodes used in this work, the MX-B will cause an issue with its considerable

thickness. Without the preparation step, the rotation angle is limited to only $[-75^\circ, 75^\circ]$ for MX-B. Hence, the sample preparation for the MX-B is a crucial step to get a high-quality result and to limit the dead-angle during the acquisition.

Regarding the sample preparation, a “free-standing” electrode was first required, which was obtained by simply peeling the porous electrode material off the current collector foil. A ZEISS laser dissection was used to precisely cut a specific pattern from the bulk electrode (see Figure 1d). The pattern along with the void around allows reducing the pathway traveling by the X-ray over a wide rotation angle $[-120^\circ, 120^\circ]$. As a result, it reduces the dead angle from 75° to 30° . Smaller dead-angles allow the use of the thicker sample (MX-B) for the experiment. It is worth mentioning that to avoid any damage of the laser beam on the region of interest, the pulse mode was used for laser beam instead of permanent mode.

Assembly of compact electrochemical cells

The assembly of the Operando cell was carried out in an argon-filled glovebox. The electrode was first introduced in the cell at the center, just above the glassy carbon window. For the MX-B, one may want to keep the patterns cut by laser beam near to the center of the windows for the ease of locating them during acquisition. Lithium foil and 1.2 M LiPF_6 (dissolved in a solvent consisting of 50% EC and 50% DMC by weight) were used as the counter electrode and the electrolyte along with Celgard 2500 as the separator. Our *Operando* cell was designed to minimize the dead angle as much as possible during the acquisition. The cells were verified to be stable for electrochemical cycling with a constant current. This cell design is also compatible with other *Operando* experiments such as X-ray diffraction in transmission.

Electrochemical cycling

All cycling tests were performed with a multipotentiostat from Biologic (France). The operational range for the NMC materials in this work is chosen between 2.5 and 4.3 V vs Li/Li^+ . Delithiation of NMC will be galvanostatically carried out under a C/10 current from pristine state to 4.3 V followed by a CV step to get a stoichiometry as uniform as possible. Then a high C-rate (1C) current will be used for the lithiation of NMC in order to enhance the limitation from porous electrode and to maximize the presence of heterogeneities. At the chosen state of lithiation, a relaxation step will be proceeded for 1 hour, and XANES-TXM data set will be collected at the end of this step. During the acquisition, 3 different energy level scans which are defined earlier, will take place.

Operando XANES tomographic data collection

The assembled cell was imaged using TXM at beamline 32-ID-C, Advanced Photon Source (APS). First, two reference spectra were collected from both pristine state and delithiation state (up to 4.3 V vs Li/Li⁺) with energy scan ranges from 8.30 keV to 8.43 keV with 150 energy steps in between. From those two reference spectra, we identified three energy levels that locate at pre-edge (8.33 keV), edge (8.58 keV), and post-edge (8.43 keV) respectively (Figure 1a). Here, in our approach, only 3 energy levels were recorded, which does not allow for the identification of all the Ni K-edge features during the operation as what proposed by Nowack *et al.*^[20] using 12 energy levels. However, our approach can significantly reduce the exposure time to X-ray of the sample as well as the duration per scan. At the end of each relaxation step, three TXM datasets at three energy levels defined earlier were collected using 721 projections over an angular range [-120°,120°] with a field of view of 50x50 μm².

Data processing

It is worth stating that the voxel size of the XANES-TXM CT measurements with our experimental setup was *ca.* 30 nm. However, to reduce the noise and the artifacts of the tomographic data in order to facilitate registration of volumes, which is crucial for the mapping of Li content, we binned the voxels of the tomographic data. Thus, the spatial resolution of the 3D volumes became lower than the single voxel size. Kimura *et al.* has investigated the effect of binning on the data processing, and they reported that there was no large difference in the magnitude of noise for the number of binned voxels more than 6×6×6. In this work, each of 7x7x7 voxels was binned, resulting in a voxel size of 210 nm. Considering the average particle size of the NMC particles ($D_{50} = 4.7 \mu\text{m}$), this spatial resolution is thought to be high enough to discuss the mesoscopic charging state distribution. The labeling of particles is implemented by the Separate Objects module of Avizo.

Registration of 2D slices between energies

In order to process the quantification of the Li concentration based on the change of the absorption coefficient at the Ni K-edge, the three TXM datasets at the three energy levels have to be spatially aligned. Image registration was performed using the *elastix* software. Following an initial rigid transformation, a nonrigid b-spline-transform is applied.

Li concentration mapping

Both the edge and peak absorption features in the Ni K edge have been shown in the literature to be approximately linearly correlated to lithiation state in NMC. Therefore, our approach was relied on the relative shift of the absorption coefficient at the Ni K-edge (at 8.35 keV). The relative shift is obtained by normalizing the 3D volume captured at the K-edge to the absorption jump calculated as a difference of the absorption coefficient at the pre-edge and the post-edge.

$$\text{MAP} = \frac{\text{Vol}_{\text{edge}} - \text{Vol}_{\text{pre-edge}}}{\text{Vol}_{\text{pre-edge}} - \text{Vol}_{\text{post-edge}}}$$

where Vol_{edge} , $\text{Vol}_{\text{pre-edge}}$, $\text{Vol}_{\text{post-edge}}$ are the 3D volumes obtained at the edge, pre-edge and post-edge of the Ni K-edge respectively.

As a result, we obtained the 3D volume that has voxels' grey level reflecting the Li concentration within the NMC particles. By combining the obtained data of NMC distribution and the Li content at corresponding voxels, we acquired the 3D charging state (Li content) map. By repeating the above procedure as lithiation proceeds, 3D lithium distribution evolution as a function of Li content in the AM can be rendered, as shown in Figure 1a.

Acknowledgements

The authors would like to acknowledge French National Association for Research and Technology (ANRT) for partially supporting the funding of this research work. T-T.N. was supported by Renault Group for his Ph.D. Project. J.X. and A.A.F. acknowledge the European Union's Horizon 2020 research and innovation program for the funding support through the European Research Council (grant agreement 772873, "ARTISTIC" project). This research used resources of the Advanced Photon Source, a U.S. Department of Energy (DOE) Office of Science User Facility operated for the DOE Office of Science by Argonne National Laboratory under Contract No. DE-AC02-06CH11357.

Declaration of Competing Interest

The authors declare no conflict of interest.

References:

- [1] J. B. Goodenough, *Journal of Solid State Electrochemistry* **2012**, *16*, 2019.
- [2] J.-M. Tarascon, *Trans. R. Soc. A* **2010**, *368*, 3227.
- [3] J. B. Goodenough, Y. Kim, *Chemistry of Materials* **2010**, *22*, 587.
- [4] J. B. Goodenough, *Energy and Environmental Science* **2014**, *7*, 14.

- [5] X. Zhang, Z. Ju, Y. Zhu, K. J. Takeuchi, E. S. Takeuchi, A. C. Marschilok, G. Yu, *Advanced Energy Materials* **2020**, 2000808.
- [6] R. Xu, Y. Yang, F. Yin, P. Liu, P. Cloetens, Y. Liu, F. Lin, K. Zhao, *Journal of the Mechanics and Physics of Solids* **2019**, 129, 160.
- [7a] M. M. Forouzan, B. A. Mazzeo, D. R. Wheeler, *Journal of The Electrochemical Society* **2018**, 165, DOI 10.1149/2.1281809jes.
- [7b] Nguyen, T., Villanova, J., Su, Z., Tucoulou, R., Fleutot, B., Delobel, B., Delacourt, C., and Demortière, A. (2021). *Adv. Energy Mater.*, 2003529. 10.1002/aenm.202003529.
- [7c] Nguyen, T.-T., Demortière, A., Fleutot, B., Delobel, B., Delacourt, C., and Cooper, S.J. (2020). *npj Computational Materials* 6. 10.1038/s41524-020-00386-4.
- [8] Y. Yang, R. Xu, K. Zhang, S. Lee, L. Mu, P. Liu, C. K. Waters, S. Spence, Z. Xu, C. Wei, D. J. Kautz, Q. Yuan, Y. Dong, Y. Yu, X. Xiao, H. Lee, P. Pianetta, P. Cloetens, J. Lee, K. Zhao, F. Lin, Y. Liu, *Advanced Energy Materials* **2019**, 9, 1900674.
- [9] X. Lu, A. Bertei, D. P. Finegan, C. Tan, S. R. Daemi, J. S. Weaving, K. B. O. Regan, T. M. M. Heenan, G. Hinds, E. Kendrick, D. J. L. Brett, P. R. Shearing, *Nature Communications* **2020**, 11, 1.
- [10] P. Pietsch, V. Wood, *Annual Review of Materials Research* **2017**, 47, 451.
- [11] V. Wood, *Nature Reviews Materials* **2018**, 3, 293.
- [12] C. Cao, M. F. Toney, T. K. Sham, R. Harder, P. R. Shearing, X. Xiao, J. Wang, *Materials Today* **2020**, 34, 132.
- [13] P. R. Shearing, D. S. Eastwood, R. S. Bradley, J. Gelb, S. J. Cooper, F. Tariq, D. J. L. Brett, N. P. Brandon, P. J. Withers, P. D. Lee, *Exploring Electrochemical Devices Using X-Ray Microscopy: 3D Micro-Structure of Batteries and Fuel Cells*, n.d.
- [14] S. R. Daemi, C. Tan, T. Volkenandt, S. J. Cooper, A. Palacios-Padros, J. Cookson, D. J. L. Brett, P. R. Shearing, **2018**, DOI 10.1021/acsaem.8b00501.
- [15] L. Almar, J. Joos, A. Weber, E. Ivers-Tiffée, *Journal of Power Sources* **2019**, 427, 1.
- [15b] Su, Z., De Andrade, V., Cretu, S., Yin, Y., Wojcik, M.J., Franco, A.A., and Demortière, A. (2020). *ACS Applied Energy Materials* 3, 4093–4102. 10.1021/acsaem.9b02236.
- [16] J. Nanda, J. Remillard, A. O'Neill, D. Bernardi, T. Ro, K. E. Nietering, J.-Y. Go, T. J. Miller, *Advanced Functional Materials* **2011**, 21, 3282.
- [17] J. Liu, M. Kunz, K. Chen, N. Tamura, T. J. Richardson, *Journal of Physical Chemistry Letters* **2010**, 1, 2120.
- [18] J. B. Leriche, S. Hamelet, J. Shu, M. Morcrette, C. Masquelier, G. Ouvrard, M. Zerrouki, P. Soudan, S. Belin, E. Elkaïm, F. Baudelet, *J. Electrochem. Soc.* **2010**, 157, A606.
- [19] G. Ouvrard, M. Zerrouki, P. Soudan, B. Lestriez, C. Masquelier, M. Morcrette, S. Hamelet, S. Belin, A. M. Flank, F. Baudelet, *Journal of Power Sources* **2013**, 229, 16.
- [20] L. Nowack, D. Grolimund, V. Samson, F. Marone, V. Wood, *Nature Publishing Group* **2016**, DOI 10.1038/srep21479.
- [21] T. Nakamura, K. Chiba, M. Fakkao, Y. Kimura, K. Nitta, Y. Terada, Y. Uchimoto, K. Amezawa, *Batteries & Supercaps* **2019**, 2, 688.
- [22] K. Chen, S. Shinjo, A. Sakuda, K. Yamamoto, T. Uchiyama, K. Kuratani, T. Takeuchi, Y. Orikasa, A. Hayashi, M. Tatsumisago, Y. Kimura, T. Nakamura, K. Amezawa, Y. Uchimoto, *Journal of Physical Chemistry C* **2019**, 123, 3292.
- [23a] J. Wang, Y.-C. K. Chen-Wiegart, C. Eng, Q. Shen, J. Wang, *Nature Communications* **2016**, 7, DOI 10.1038/ncomms12372.

- [23b] Su, Z., Decencière, E., Nguyen, T.-T., El-Amiry, K., De Andrade, V., Franco, A.A., and Demortière, A. (2022). *npj Comput Mater* **8**, 30. 10.1038/s41524-022-00709-7.
- [24] D. P. Finegan, A. Vamvakeros, C. Tan, T. M. M. Heenan, S. R. Daemi, N. Seitzman, M. Di Michiel, S. Jacques, A. M. Beale, D. J. L. Brett, P. R. Shearing, K. Smith, *Nature Communications* **2020**, DOI 10.1038/s41467-020-14467-x.
- [25] C. Tan, A. S. Leach, T. M. M. Heenan, H. Parks, R. Jervis, J. N. Weker, D. J. L. Brett, P. R. Shearing, *Cell Reports Physical Science* **2021**, 100647.
- [26] Y. Kimura, A. Tomura, M. Fakkao, T. Nakamura, N. Ishiguro, O. Sekizawa, K. Nitta, T. Uruga, T. Okumura, M. Tada, Y. Uchimoto, K. Amezawa, *J. Phys. Chem. Lett.* **2020**, *11*, 3629.
- [27] Y. S. Yu, M. Farmand, C. Kim, Y. Liu, C. P. Grey, F. C. Strobridge, T. Tyliczszak, R. Celestre, P. Denes, J. Joseph, H. Krishnan, F. R. N. C. Maia, A. L. D. Kilcoyne, S. Marchesini, T. P. C. Leite, T. Warwick, H. Padmore, J. Cabana, D. A. Shapiro, *Nature Communications* **2018**, DOI 10.1038/s41467-018-03401-x.
- [28] W. E. Gent, Y. Li, S. Ahn, J. Lim, Y. Liu, A. M. Wise, C. B. Gopal, D. N. Mueller, R. Davis, J. N. Weker, J.-H. Park, S.-K. Doo, W. C. Chueh, *Advanced Materials* **2016**, *28*, 6631.
- [29] Z. Su, T.-T. Nguyen, C. Le Bourlot, F. Cadiou, A. Jamali, V. De Andrade, A. A. Franco, A. Demortière, *Chemistry–Methods* **2022**, *2*, e202100051.
- [30] S.-M. Bak, E. Hu, Y. Zhou, X. Yu, S. D. Senanayake, S.-J. Cho, K.-B. Kim, K. Y. Chung, X.-Q. Yang, K.-W. Nam, *ACS Applied Materials & Interfaces* **2014**, *6*, 22594.
- [31] W. S. Yoon, M. Balasubramanian, K. Y. Chung, X. Q. Yang, J. McBreen, C. P. Grey, D. A. Fischer, *Journal of the American Chemical Society* **2005**, *127*, 17479.
- [32] A. Deb, U. Bergmann, S. P. Cramer, E. J. Cairns, *Journal of Applied Physics* **2005**, *97*, 113523.
- [33] O. J. Borkiewicz, K. M. Wiaderek, P. J. Chupas, K. W. Chapman, **2015**, DOI 10.1021/ACS.JPCLETT.5B00891.
- [34] O. J. Borkiewicz, B. Shyam, K. M. Wiaderek, C. Kurtz, P. J. Chupas, K. W. Chapman, *Journal of Applied Crystallography* **2012**, *45*, 1261.
- [35] Z. Jiang, J. Li, Y. Yang, L. Mu, C. Wei, X. Yu, P. Pianetta, K. Zhao, P. Cloetens, F. Lin, Y. Liu, *Nature Communications* **2020**, *11*, 1.
- [36] A. Mistry, T. Heenan, K. Smith, P. Shearing, P. P. Mukherjee, *ACS Energy Lett.* **2022**, *7*, 1871.
- [37] D. J. Miller, C. Proff, J. G. Wen, D. P. Abraham, J. Bareño, *Advanced Energy Materials* **2013**, *3*, 1098.

Supporting information

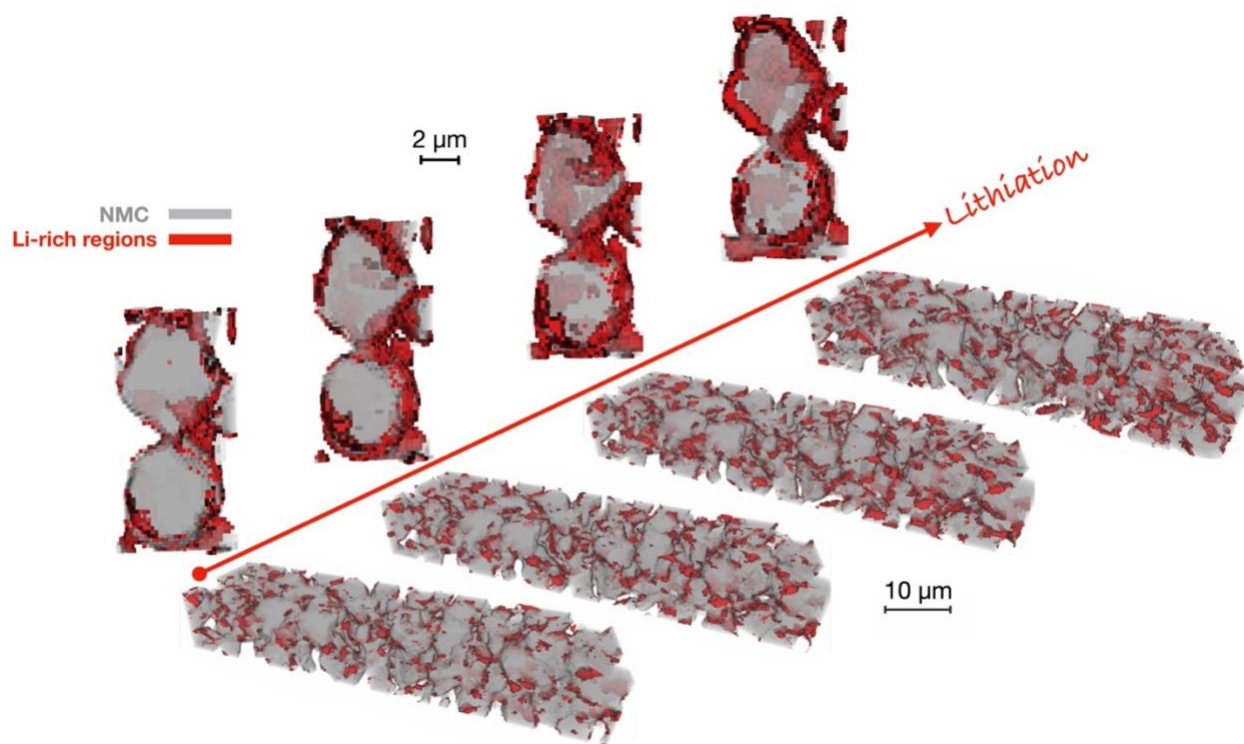


Figure S1: The detachment of the AM particles between two TXM acquisitions.

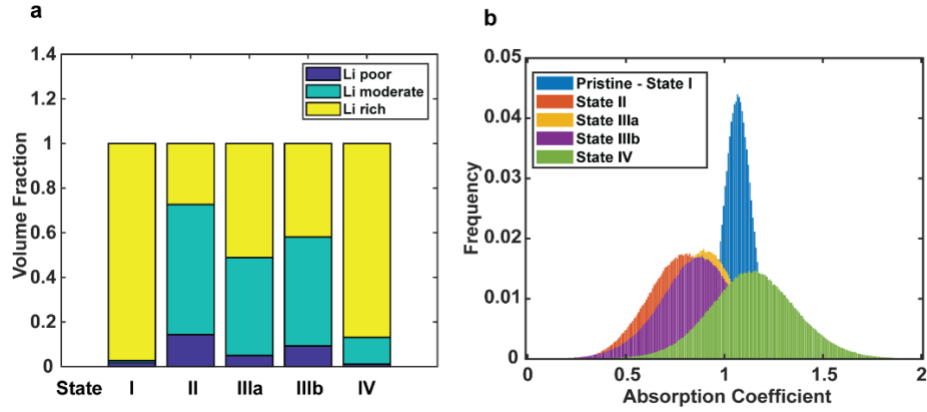


Figure S2: a. The bar graph represents the volume fraction of AM with different Li contents obtained from 3D quantitative analysis. b. The distribution of absorption coefficient at each voxel within the volume.

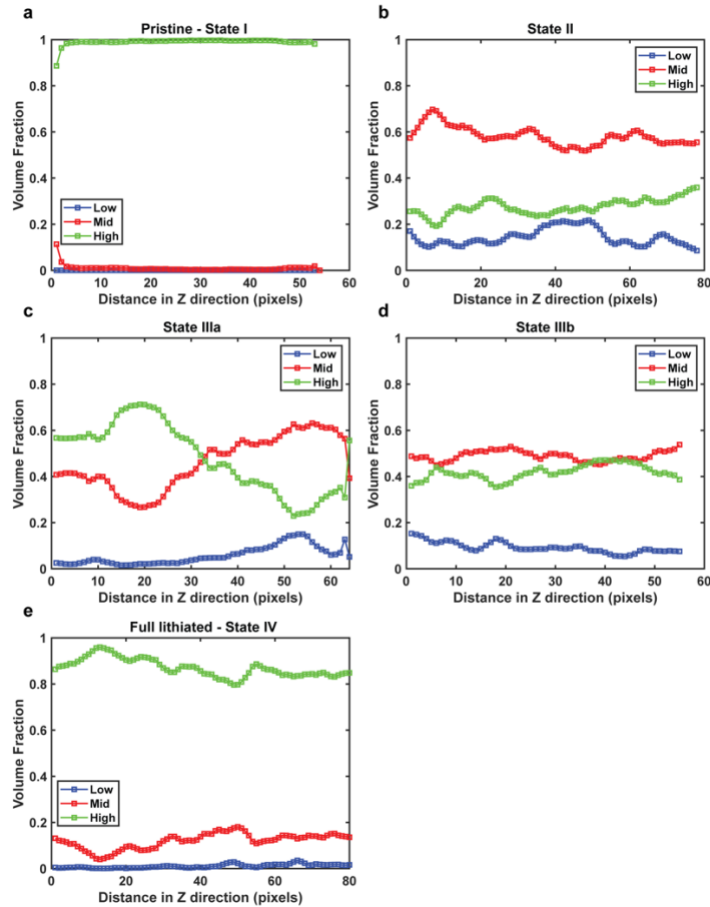


Figure S3. The volume fraction profiles along the Z-axis direction (through-plane) of the electrode. Each point was obtained by calculating the fraction of the phase in a 2D slice across the Z-axis. a. State I (Pristine electrode). b. State II (CCCV charge to 4.3 V). c-d. Discharge 1C to 50% DoD captured at position 1 and 2, respectively. e. State III (CCCV discharge to 2.5 V).

